A MAGNETICALLY SUSPENDED, SPHERICAL PERMANENT MAGNETIC DIPOLE ACTUATOR

Tyler T. Hamer[1], Minkyun Noh[1], Lei Zhou[1], Joshua Chabot[2], and David L. Trumper[1]
[1]Department of Mechanical Engineering
Massachusetts Institute of Technology
Cambridge, MA, USA
[2]MIT Lincoln Laboratory
Lexington, MA, USA

INTRODUCTION

The attitude control system (ACS) of a spacecraft contains a minimum of three reaction wheels to rotate the spacecraft in 3 degrees of freedom (DoF), but typically contains additional reaction wheels for both redundancy and improved pointing accuracy. Each wheel rotates the spacecraft about its axis by imparting an equal-and-opposite torque when the spacecraft accelerates the wheel. Since space, weight, and power (SWaP) are a premium on a spacecraft, reaction spheres, which impart an equal-and-opposite torque about an arbitrary axis when the spacecraft accelerates the sphere about that axis, have been proposed to reduce the ACS down to a single device.

While NASA first proposed reaction spheres over a half century ago, limitations with previous designs have kept the technology from commercialization [1]. These designs can be generalized into two categories: asynchronous, induction-type actuators and synchronous actuators similar to DC and hysteresis motors. The induction-type designs are difficult to model and suffer from eddy current losses in the rotor while the synchronous designs often have rotors constructed from multiple magnets which presents fabrication, strength, and balance issues. To incorporate the best of both worlds, the mechanical simplicity of an induction motor with the efficiency and simple model of a brushless DC motor, a spherical permanent magnetic dipole rotor actuated by a stator of surrounding coils has been considered [2, 3]. This paper presents the modeling, design, and vertical suspension of a prototype permanent magnetic dipole reaction sphere depicted in Figure 1.

OPERATING PRINCIPLE

Torque and force on the dipole rotor arise from the interaction of the rotor's external magnetic field with the current passing through each coil. Since the rotor is a magnetic dipole, the torque ${}^{\mathrm{c}}\boldsymbol{T}_{\mathrm{r}}$ and force ${}^{\mathrm{c}}\boldsymbol{F}_{\mathrm{r}}$ on the rotor by a single coil can be found by approximating the coil as a magnetic dipole as well.

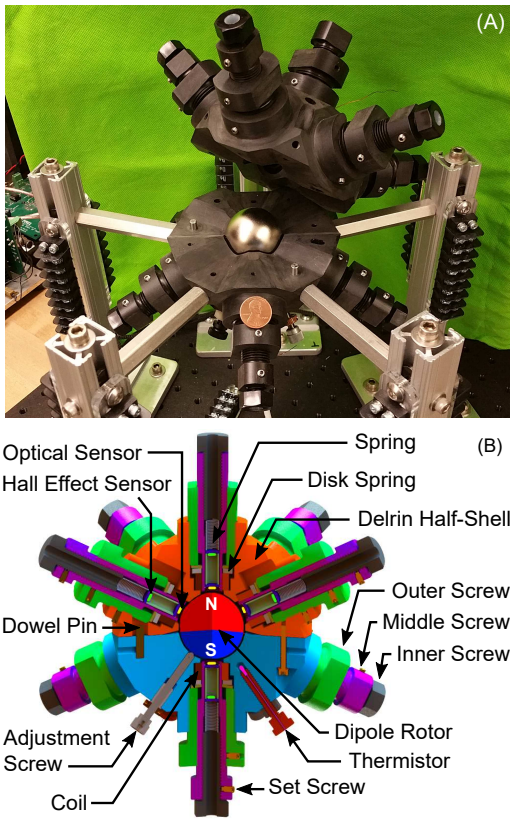

FIGURE 1. Permanent magnetic dipole reaction sphere (a) bench-level prototype with (b) label cross section.

The torque and force between these two magnetic dipoles are

$$ {}^{\mathrm{c}}\boldsymbol{T}_{\mathrm{r}} = -\left(\boldsymbol{m}_{\mathrm{c}} \times \boldsymbol{B}_{\mathrm{r}}\right) \tag{1a} $$

$$ {}^{\mathrm{c}}\boldsymbol{F}_{\mathrm{r}} = -\bigtriangledown\left(\boldsymbol{m}_{\mathrm{c}} \cdot \boldsymbol{B}_{\mathrm{r}}\right), \tag{1b} $$

where $\boldsymbol{B}_{\mathrm{r}}$ is the external magnetic flux density of the rotor and and $\boldsymbol{m}_{\mathrm{c}}$ is the approximated magnetic dipole moment of the coil.

The external magnetic flux density of the rotor is the magnetic flux density of a dipole $\boldsymbol{B}_{\mathrm{dipole}}$:

$$ \boldsymbol{B}_{\mathrm{dipole}}(\boldsymbol{r}) = \frac{\mu_0}{4\pi}\left[\frac{3\boldsymbol{r}\left(\boldsymbol{m}_{\mathrm{dipole}} \cdot \boldsymbol{r}\right)}{|\boldsymbol{r}|^5} - \frac{\boldsymbol{m}_{\mathrm{dipole}}}{|\boldsymbol{r}|^3}\right], \tag{2} $$

which in spherical coordinates is

$$\boldsymbol{B}_{\text{dipole}}(\boldsymbol{r}) = \frac{\mu_0}{4\pi}\frac{|\boldsymbol{m}_{\text{dipole}}|}{|\boldsymbol{r}|^3}\left(2\cos\theta\hat{\boldsymbol{i}}_{\boldsymbol{r}} + \sin\theta\hat{\boldsymbol{i}}_{\boldsymbol{\theta}}\right), \quad (3)$$

where μ_0 is the permeability of free space and $\boldsymbol{m}_{\text{dipole}}$ is the magnetic dipole moment. $\boldsymbol{r}$ is the position of the point of interest with respect to the center of the magnetic dipole, which in this case will be the position of the center of the coil's approximated dipole with respect to the rotor's center ${}^{\text{r}}\boldsymbol{r}_{\text{c}}$.

The magnetic dipole moment of the rotor $\boldsymbol{m}_{\text{r}}$ is

$$\boldsymbol{m}_{\text{r}} = \mathcal{V}_{\text{r}}\frac{B_{\text{rem}}}{\mu_0}\boldsymbol{n}_{\text{r}}, \quad \mathcal{V}_{\text{r}} = \frac{4}{3}\pi R_{\text{r}}^3, \quad (4)$$

where $\mathcal{V}_{\text{r}}$, R_{r}, and B_{rem}, are the rotor's volume, radius, and remanence respectively, and $\boldsymbol{n}_{\text{r}}$ is a unit vector along the rotor's axis of magnetization. The approximated magnetic dipole moment of the coil is

$$\boldsymbol{m}_{\text{c}} = N i_{\text{c}} A_{\text{ave}} \boldsymbol{n}_{\text{c}}, \quad (5)$$

where N is the coil's number of turns, i_{c} is the current through the coil, A_{ave} is the average area enclosed by each turn, and $\boldsymbol{n}_{\text{c}}$ is a unit vector along the coil's axis.

Substituting Equations (2), (4) and (5) into Equation (1) for when the rotor's center lies along the coil's axis (${}^{\text{r}}\boldsymbol{r}_{\text{c}}/|{}^{\text{r}}\boldsymbol{r}_{\text{c}}| = \boldsymbol{n}_{\text{c}}$), the torque and force on the rotor by a single coil are

$${}^{\text{c}}\boldsymbol{T}_{\text{r}} = K_{\text{T}} i_{\text{c}}(\boldsymbol{n}_{\text{c}} \times \boldsymbol{n}_{\text{r}}) \quad (6a)$$

$${}^{\text{c}}\boldsymbol{F}_{\text{r}} = \frac{1}{2}K_{\text{F}} i_{\text{c}}[3(\boldsymbol{n}_{\text{r}} \cdot \boldsymbol{n}_{\text{c}})\boldsymbol{n}_{c} - \boldsymbol{n}_{\text{r}}], \quad (6b)$$

where K_{T} and K_{F} are respectively the reaction sphere's torque and force constants for a single coil while the rotor's center lies along that coil's axis:

$$K_{\text{T}} = \frac{\mu_0 |\boldsymbol{m}_{\text{r}}| |\boldsymbol{m}_{\text{c}}|}{4\pi |{}^{\text{r}}\boldsymbol{r}_{\text{c}}|^3 i_{\text{c}}} = \frac{1}{3} N A_{\text{ave}} B_{\text{rem}} \left(\frac{R_{\text{r}}}{|{}^{\text{r}}\boldsymbol{r}_{\text{c}}|}\right)^3 \quad (7a)$$

$$K_{\text{F}} = \frac{3\mu_0 |\boldsymbol{m}_{\text{r}}| |\boldsymbol{m}_{\text{c}}|}{2\pi |{}^{\text{r}}\boldsymbol{r}_{\text{c}}|^4 i_{\text{c}}} = \frac{2N A_{\text{ave}} B_{\text{rem}}}{R_{\text{r}}} \left(\frac{R_{\text{r}}}{|{}^{\text{r}}\boldsymbol{r}_{\text{c}}|}\right)^4 . \quad (7b)$$

The overall torque ${}^{\text{c}_{\text{tot}}}\boldsymbol{T}_{\text{r}}$ and force ${}^{\text{c}_{\text{tot}}}\boldsymbol{F}_{\text{r}}$ on the rotor are the superposition of the individual torques and forces from each coil. For a rotor centered within a radial array of identical surrounding coils (thus the rotor's center lies along each coil's axis), these are

$${}^{\text{c}_{\text{tot}}}\boldsymbol{T}_{\text{r}} = \sum_{a=1}^{b} {}^{\text{c}_b}\boldsymbol{T}_{\text{r}} = K_{\text{T}} \sum_{a=1}^{b} i_{\text{c}_b}(\boldsymbol{n}_{\text{c}_b} \times \boldsymbol{n}_{\text{r}}) \quad (8a)$$

$${}^{\text{c}_{\text{tot}}}\boldsymbol{F}_{\text{r}} = \sum_{a=1}^{b} {}^{\text{c}_b}\boldsymbol{F}_{\text{r}} = \frac{1}{2}K_{\text{F}} \sum_{a=1}^{b} i_{\text{c}_b}\left[3(\boldsymbol{n}_{\text{r}} \cdot \boldsymbol{n}_{\text{c}_b})\boldsymbol{n}_{\text{c}_b} - \boldsymbol{n}_{\text{r}}\right]. \quad (8b)$$

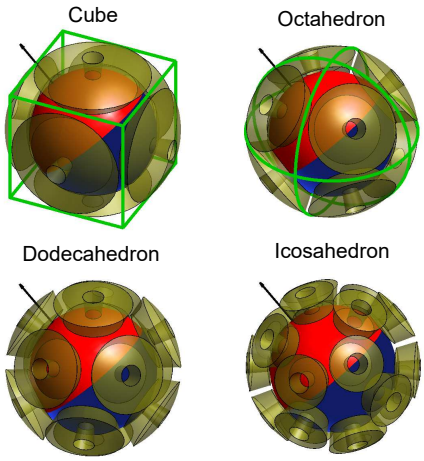

FIGURE 2. Distributions of coils centered on faces of platonic solids. Green lines represent singular dipole orientations (3 DoF suspension of dipole rotor is lost) for cube and octahedron configurations.

In order to maintain symmetry, radial arrays corresponding to the coils centered on the faces of platonic solids are considered. Applying Equation (8) over these distributions, a minimum of 12 equidistant coils is needed for full 3 DoF magnetic suspension of the dipole rotor independent of the rotor's orientation as visualized in Figure 2.

BENCH-LEVEL PROTOTYPE DESIGN

Figure 1 depicts the reaction sphere bench level prototype with a labeled cross section. Twelve equidistantly distributed coils levitate and rotate the dipole rotor while 12 optical sensors and 12 Hall effect sensor, coaxially placed within each coil, measure the rotor's position and the orientation of the rotor's dipole respectively. These position and rotation measurements are fed back to a real-time controller which drives 12 transconductance power amplifiers, each which drive a coil. The design of the actuation, sensing, mechanical structure, power electronics, and controller are described below.

Actuation

The dipole rotor is a 38.1 mm (1.5 in) diameter, permanently axially magnetized, NdFeB (Grade 42) sphere (K&J Magnetics SX8) with a mass of M_{r} = 0.22 kg and remanence of B_{rem} = 1.31 T. The stator consists of two mating, symmetric Delrin half-shells, which together form a dodecahedron with a 40.1 mm diameter spherical pocket that the rotor is contained in. Twelve equidistantly distributed cylindrical coils, one centered on each face of the dodecahedron stator at a diameter of 42.1 mm, levitate and rotate the rotor. Thus when the rotor is centered within the spherical pocket, the prototype has a 1 mm mechanical air gap and 2 mm magnetic air gap and the rotor can translate up to $\pm$1 mm in 3 DoF.

TABLE 1. Actuation Key Parameters.

Symbol	Parameter	Value
M_{r}	rotor mass	0.22 kg
B_{rem}	rotor remanence	1.31 T
R_{r}	rotor radius	19.05 mm
$\lvert{}^{\mathrm{r}}\boldsymbol{r}_{\mathrm{c}}\rvert$	rotor-coil center distance	26.6 mm
N	coil turns	348
A_{ave}	turn average enclosed area	201 mm^2
K_{T}	single-coil torque constant	11.2 mN·m/A
K_{F}	single-coil force constant	2.52 N/A

Each cylindrical coil is wound from N = 348 turns of 0.3 mm diameter (AWG 28) magnet wire making a footprint of 20 mm outer-diameter $\times$ 12 mm inner-diameter $\times$ 10 mm long. The average area enclosed by a turn of each coil is A_{ave} = 201 mm^2. Additionally, each coil has a series self-inductance of L_{s} = 1.6 mH and a series resistance of R_{s} = 4.1 Ω as measured at 100 Hz by an Agilent 4284A LCR meter. When the rotor is centered, FEMM simulation determined an effective distance between the rotor's center and the center of each coil's effective dipole is $\lvert{}^{\mathrm{r}}\boldsymbol{r}_{\mathrm{c}}\rvert$ = 26.6 mm. Substituting these values into Equation (7), the torque constant and force constant of each coil are estimated to be K_{T} = 11.2 mN·m/A and K_{F} = 2.52 N/A respectively, requiring a predicted 0.84 A for 1 DoF suspension by a single coil directly above the rotor. The key parameters for actuation are summarized in Table 1.

Sensing

The stator contains 12 equidistantly distributed sensing modules, one coaxially placed within each of the coils, for feedback. Each sensing module consists of a reflective optical sensor (Fairchild QRE1113GR) for measuring the translational position of the rotor and a Hall effect sensor (Allegro A1308KUA-1-T) for measuring the orientation of the rotor's dipole (rotational position). Within each sensing module, each sensor is mounted on its own printed circuit board (PCB) spaced 15 mm apart. This allows the optical sensor to be positioned about 1 mm from the rotor when closest for highest sensitivity and the Hall effect sensor to be positioned at least 15 mm from the rotor when closest to avoid saturation. When the rotor is centered, the prototype has an optical sensing air gap of 2 mm and a Hall effect sensing air gap of 17 mm.

The sensitivity of the optical sensor and the Hall effect sensor with respect to the rotor's position and orientation of its dipole are provided in Figure 3. To measure these sensitivities, a sensor module is mounted to an aluminum spacer above a steel XY linear stage (Newport 461-XY-M) and a steel Z linear stage (by Oriel Corporation) with the rotor

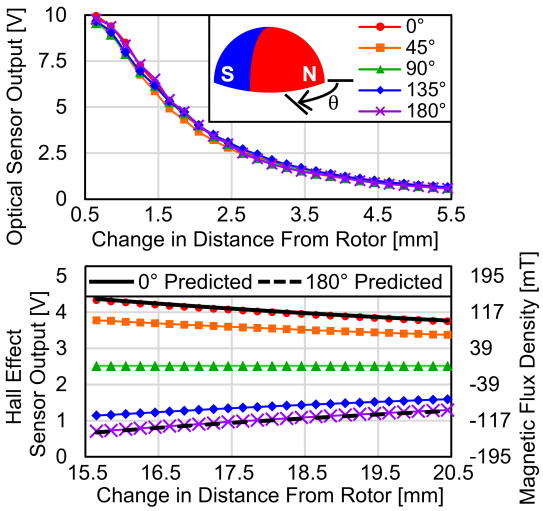

FIGURE 3. Measured sensor module (optical sensor and Hall effect sensor) voltage as functions of the rotor's translation and rotation of its dipole.

mounted on an aluminum spacer above a steel rotary stage (Melles Griot 98 mm dia. stage) across from it. The aluminum spacers keep the rotor at least 50 mm from the stages to ensure the stages' steel does not distort the rotor's dipole magnetic field. The Y-and Z-axes orient the sensor module radially with the rotor. Then the rotary stage sets the dipole's orientation and the X-axis moves the sensor module radially.

With the 0° orientation denoting the rotor's north pole facing the sensor module, the rotary stage indexes the rotor in 45° increments. For each orientation of the rotor's dipole, the X-axis steps the sensor module from 0.65 mm to 20.5 mm from the rotor's surface in 20 μm increments. At each position, the voltage of both sensors are acquired with a sampling rate of 10 kHz using a National Instruments (NI) PXI-6289 M-Series analog input card of 750 kHz bandwidth, 18 bit resolution, and an input range of $\pm$10 V for the optical sensor and $\pm$5 V for the Hall effect sensor.

The optical sensor's voltage did not vary with the dipole's orientation, but varied as a cubic polynomial with its distance from the rotor. Linearized about the optical sensor's distance from a centered rotor (2 mm), the optical sensor has a sensitivity of H_{opt} = 2.75 V/mm. The Hall effect sensor's voltage varied sinusoidally with the dipole's orientation and as a cubic inverse with its distance from the rotor just like the radial component of the rotor's magnetic flux density in Equation (3). Thus the Hall effect sensor's voltage varied linearly with the radial component of the rotor's magnetic flux density with a sensitivity of H_{Hall} = 12.8 V/T.

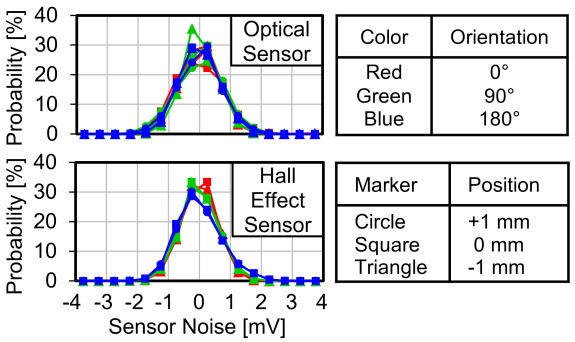

FIGURE 4. Histograms of senor module noise.

Using the same setup, each sensor's noise level is measured over a period of 10 sec for the 0°, 90°, and 180° orientations of the rotor's dipole at distances from the rotor corresponding to the rotor's -1 mm, 0 mm, and +1 mm positions. Figure 4 shows histograms for these 9 stationary configurations. Both sensor's noise levels are Gaussian distributed and independent of the dipole's orientation and distance from the rotor. The optical sensor's voltage noise has a standard deviation of 0.67 mV, 9 times larger than the quantization error, corresponding to a position noise standard deviation of 0.24 μm. The Hall effect sensor's voltage noise has a standard deviation of 0.61 mV, 16 times larger than quantization error, corresponding to a magnetic flux density noise standard deviation of 48 μT.

Mechanical Design

The stator consists of two mating, symmetric Delrin half-shells. The bottom half-shell is held up by 5 standoffs running to 80-20 pillars mounted to an optical breadboard. These half-shells are made from Delrin as eddy currents formed from the rotor rotating in metal half-shells would shield the Hall effect sensors. Further, the surface of spherical pocket can then be used as a touch down bearing. To ensure the Delrin does not overheat, four embedded thermistors monitor the stator's temperature.

The rotor can be easily placed within or removed from the stator by separating the two half-shells. To ensure the half-shells mate in a repeatable fashion, the mating surfaces use two dowel pins, one in a slot and the other in a hole. The position of the rotor within the stator's spherical pocket can be manually adjusted externally using 3 adjustment screws within the stator. This allows the rotor's rotation to be tested separately from its suspension if needed.

To coaxially place each sensing module within its accompanying coil, but allow for radial adjustment if needed, a series of three hollow screws is used. The inner screw provides clearance for the sensing module's wires and with a spring, preloads the sensing module against a retaining ring in the middle screw. The outer screw with a plastic disk spring, preloads the coil into a radial pocket centered on one of the stator's 12 outer faces. The middle screw translates along the coil's inner bore and outer screw, positioning the sensing module radially while keeping the module in coaxial alignment with the coil. Set screws in the stator and two outer screws later lock each hollow screw into place.

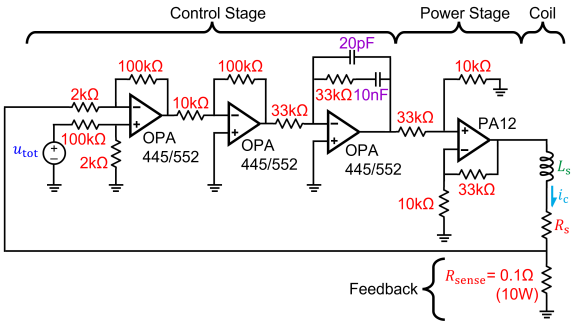

FIGURE 5. Circuit diagram for power amplifier with a DC gain of 0.2 A/V and 5 kHz bandwidth [4].

Power Electronics

Each coil is driven by its own transconductance linear power amplifier, whose circuit is provided in Figure 5. These amplifiers were previously used to drive a bearingless hysteresis motor [4] and later adjusted for use with these coils. A sense resistor of R_s = 0.1 Ω feeds back the current through the coil i_c to a control stage containing of 3 high-voltage op amps (Texas Instruments OPA 445 or OPA 552) to provide PI compensation. The control stage drives a power stage containing a linear power amplifier (Apex Microtechnology PA12) with a gain in the feedback path below 0.25 for stability. The entire circuit drives current through the coil with a DC transconductance gain of G_p = 0.2 A/V and a bandwidth of 5 kHz.

Controller

Signals from the 12 sensing modules are acquired using two NI PXI-6289 M-Series analog input cards. These are fed back to a control algorithm implemented in LabVIEW on a NI PXIe-8135 embedded controller and used to drive the 12 power amplifiers, and in turn their corresponding coils, via an NI PXIe-6739 dedicated analog output card. For initial testing, a control algorithm running at 2 kHz levitates the rotor using a single coil directly above the rotor via feedback from the optical sensor in that coil's coaxial sensing module. The coil above the rotor is used as the other DoF besides rotation about the dipole are passively stable. Figure 6 shows the block diagram for this control system.

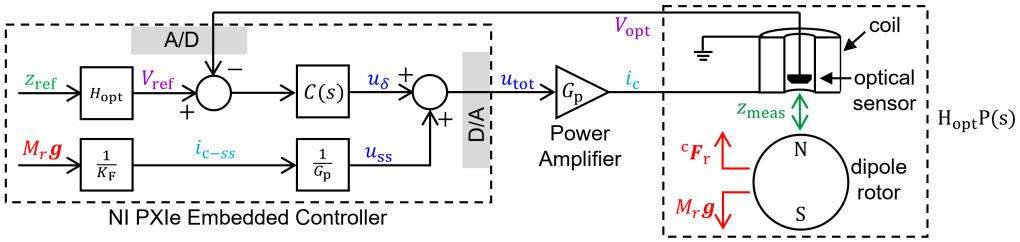

FIGURE 6. Block diagram for vertical suspension of the dipole rotor by the coil and optical sensor above it.

The rotor's weight passes through the inverse of the single-coil motor constant for a centered rotor to generate the single-coil steady state bias current, a predicted $i_{\text{c-ss}}$ = 0.84A. The bias current then passes through the inverse of the power amplifier's DC gain to generate the steady state bias control effort u_{ss} to compensate for the rotor's weight. This control effort is added to the small displacement control effort u_δ responsible for compensating for rotor's small vertical deviations from the center.

The small displacement control effort is generated by a lead compensator $C(s)$ from the difference between the rotor's desired vertical position z_{ref} (0 mm corresponding to a centered rotor) and the rotor's vertical position measured by the optical sensor z_{meas}. To design the lead compensator, a linearized dynamic model $P(s)$ for the rotor's vertical position from the center z with respect to small changes in the current through the coil $i_{\text{c-}\delta}$ is built. It is represented by the following transfer function:

$$P(s) = \frac{z}{i_{\text{c-}\delta}} = \frac{K_{\text{F}}}{k}\left(\frac{k/M_{\text{r}}}{s^2 - k/M_{\text{r}}}\right), \tag{9}$$

where k is the negative stiffness of the centered rotor's vertical suspension given by

$$k = 4K_{\text{F}} i_{\text{c-ss}} / \left|{}^{\text{r}}\boldsymbol{r}_{\text{c}}\right|. \tag{10}$$

Substituting in the actuation key values, the rotor's suspension instability has a predicted break frequency of $\sqrt{k/M_{\text{r}}}$ = 6.1 Hz.

Using this model, the DC gain of the transconductance amplifier, and the sensitivity of the optical sensor, the following lead compensation is used to crossover at a predicted ω_{c} = 60 Hz with a predicted phase margin of ϕ_{M} = 25°:

$$C(s) = K_{\text{p}}\frac{\alpha\tau_{\text{d}}s + 1}{\tau_{\text{d}}s + 1}, \tag{11}$$

where K_{p} = 14.8, α = 3, and τ_{d} = 0.0015 sec.

INITIAL EXPERIMENTATION & RESULTS

Using the controller above, the rotor is successfully levitated in the center of the stator's spherical pocket by the coil above it. The single-coil steady state bias current is measured to be $i_{\text{c-ss}}$ = 0.86A corresponding to a single-coil motor force constant of K_{F} = 2.45 N/A. Both of these values are within 3% of their predicted values. The performance of the rotor's vertical suspension is evaluated in both the frequency and time domain. Table 2 summarizes the overall performance.

TABLE 2. Vertical Suspension Performance.

Symbol	Parameter	Predicted	Measured
$i_{\text{c-ss}}$	bias current	0.84 A	0.86 A
K_{F}	force constant	2.52 N/A	2.45 N/A
$\sqrt{k/M_{\text{r}}}$	instability freq.	6.1 Hz	6.7 Hz
ω_{c}	crossover freq.	60 Hz	50-64 Hz
ϕ_{M}	phase margin	25°	10-22°

Frequency Response

To evaluate the rotor's vertical suspension in the frequency domain, the rotor's desired vertical position is varied sinusoidally with an amplitude of 50 μm over 170 frequencies from 1 Hz to 1 kHz. At each of these frequencies, the frequency response of the rotor's linearized dynamic model $P(s)$, the loop return ratio $RR(s) = C(s)G_{\text{p}}P(s)H_{\text{opt}}$, and the closed loop $RR(s)/[1 + RR(s)]$ is measured. Each of these measured frequency responses along with their corresponding predicted frequency responses are displayed as Bode plots in Figure 7.

The measured frequency response of the rotor's dynamics has a break frequency for its instability of $\sqrt{k/M_{\text{r}}}$ = 6.7 Hz. Additionally, its magnitude unexpectedly drops at 50 Hz until 250 Hz where it recovers after passing through a notch-and-peak pair. This pair implies a pair of complex-zeros and-poles so it is hypothesized that this magnitude drop-then-recover occurs from the stator's mass coupling to and then decoupling from the rotor's mass. This magnitude drop has two effects: (1) It causes the return ratio to crossover through unity magnitude at a measured ω_{c} = 50 Hz with a measured phase margin of ϕ_{M} = 10°, both lower than expected. (2) Since the drop is near crossover, it distorts the closed loop magnitude's resonance peak.

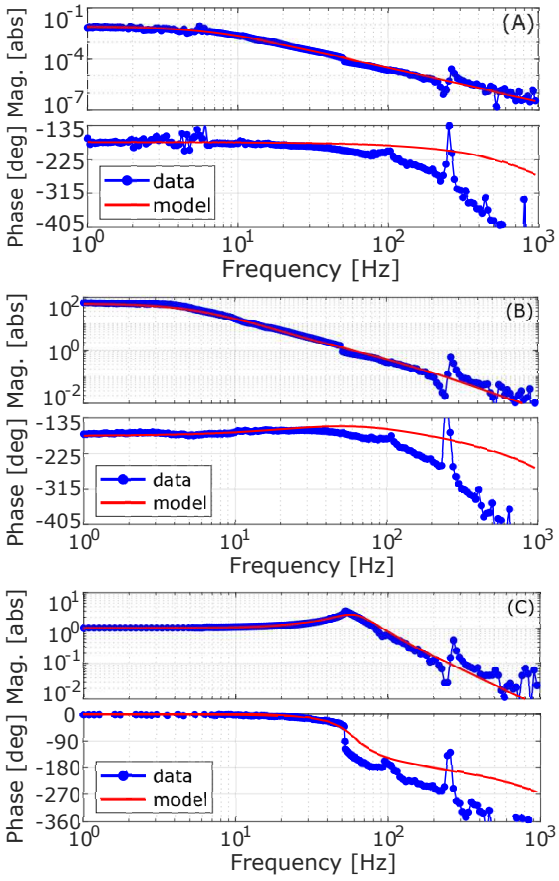

FIGURE 7. Frequency response of (a) the rotor dynamics, (b) return ratio, and (c) closed loop during vertical suspension of the rotor by the coil above it.

Time Response

To evaluate the rotor's vertical suspension in the time domain, the rotor's desired position is stepped 100 μm from -50 μm to 50 μm. Figure 8 shows the rotor's response to this step. The rotor steps 104 μm, peaking in 8.0 ms with 49% overshoot and settling in 51.7 ms. These correspond to a measured ω_c = 64 Hz with a measured phase margin of ϕ_M = 22°, similar to the frequency domain evaluation.

CONCLUSION

Reducing space, weight, and power (SWAP) is essential in the design of spacecraft. One possible way to reduce SWAP is to replace the three reaction wheels of a spacecraft's ACS with a single reaction sphere. This paper presents a spherical permanent magnetic dipole rotor driven by 12 surrounding equidistant coils for consideration as a reaction sphere. Such a design has a mechanically simple rotor like induction motors with the model simplicity of hysteresis-and brushless DC-motors. In fact, it was shown that the torque and force on the rotor can be modeled as the superposition of the torque and force generated by 12 sets of two dipoles.

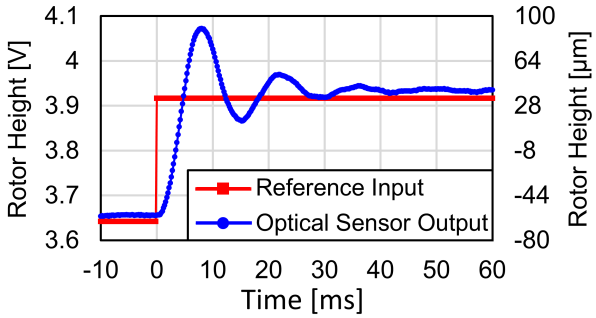

FIGURE 8. Step response of sphere's height for a 100 μm input step.

After presenting the reaction sphere's actuation, the sensing, mechanical structure, power electronics, and controller were presented. The design uses 12 sets of optical sensors and Hall effects sensors, placed coaxially with in each coil, to provide position and rotation feedback respectively. This design was physically constructed. Using a lead compensator, the coil above the rotor successfully levitated the rotor by itself with position feedback from the coil's coaxial optical sensor. The rotor required 0.86 A to levitate corresponding to a force constant per coil of 2.45 N/A while the rotor is centered. The frequency response and the step response of the rotor were measured to evaluate the suspension. The suspension was found to crossover just below 60 Hz, well above the 6.7 Hz instability of the rotor's dynamics, with a phase margin around 16°. Next steps involve testing 1 DoF rotation and then 3 DoF-suspension and-rotation separately, then together.

ACKNOWLEDGMENTS

This work is performed in collaboration with and supported by MIT Lincoln Laboratory.

REFERENCES

[1] Zhu L, Guo J, Gill E. Review of reaction spheres for spacecraft attitude control. Progress in Aerospace Sciences. 2017 May;91:67–86.

[2] Wang J, Jewell GW, Howe D. Analysis, design and control of a novel spherical permanent-magnet actuator. IEE Proceedings - Electric Power Applications. 1998 January;145(1):61–71.

[3] Chabot J. A Spherical Magnetic Dipole Actuator for Spacecraft Attitude Control [Master's Thesis]. Aerospace Engineering Sciences, University of Colorado. Boulder, CO; 2015.

[4] Noh M, Gruber W, Trumper DL. Hysteresis Bearingless Slice Motors With Homopolar Flux-Biasing. IEEE/ASME Transactions on Mechatronics. 2017;22(5):2308–2318.